



Driving Mechanisms of Double-Nosed Low-Level Jets during MATERHORN Experiment

LUIGI BROGNO,^a FRANCESCO BARBANO,^a LAURA SANDRA LEO,^{a,b} HARINDRA J. S. FERNANDO,^b AND SILVANA DI SABATINO^a

^a *Physics and Astronomy Department, University of Bologna, Bologna, Italy*

^b *Department of Civil and Environmental Engineering and Earth Sciences, University of Notre Dame, Notre Dame, Indiana*

(Manuscript received 12 September 2020, in final form 19 July 2021)

ABSTRACT: In the realm of boundary layer flows in complex terrain, low-level jets (LLJs) have received considerable attention, although little literature is available for double-nosed LLJs that remain not well understood. To this end, we use the Mountain Terrain Atmospheric Modeling and Observations (MATERHORN) dataset to demonstrate that double-nosed LLJs developing within the planetary boundary layer (PBL) are common during stable nocturnal conditions and present two possible mechanisms responsible for their formation. It is observed that the onset of a double-nosed LLJ is associated with a temporary shape modification of an already-established LLJ. The characteristics of these double-nosed LLJs are described using a refined version of identification criteria proposed in the literature, and their formation is classified in terms of two driving mechanisms. The wind-driven mechanism encompasses cases where the two noses are associated with different air masses flowing one on top of the other. The wave-driven mechanism involves the vertical momentum transport by an inertial-gravity wave to generate the second nose. The wave-driven mechanism is corroborated by the analysis of nocturnal double-nosed LLJs, where inertial-gravity waves are generated close to the ground by a sudden flow perturbation.

KEYWORDS: Inertia-gravity waves; Surface fluxes; Valley/mountain flows; Mountain meteorology; Complex terrain; Boundary layer

1. Introduction

The low-level jet (LLJ) is a strong and narrow airstream typically observed within the planetary boundary layer (PBL) (Stull 1988). The LLJ wind speed profile usually takes the shape of a nose, namely, a maximum with a fast decay of the wind speed with height both below and above it. Deviations from this “canonical” shape have been observed in the literature, consisting of wind speed profiles with two noses simultaneously observed along the vertical. These “atypical” LLJs will be referred to as double-nosed LLJs in the current study, although the term multiple LLJ is sometimes used when more noses are present (e.g., Banta et al. 2002; Tuononen et al. 2017).

Despite no field campaigns have been conducted to specifically study double-nosed LLJs, several investigations have reported on their occurrences, mostly in flat and rarely in complex terrain. Typically observed over the Great Plains of the United States, nocturnal double-nosed LLJs developing in flat terrain mostly occurred within the first 400–600 m AGL (Banta et al. 2002;

Pichugina et al. 2007; Banta 2008), with sporadic cases within 1300–1600 m AGL (Klein et al. 2015). Their frequency has been rarely reported, with Pichugina et al. (2007) recording double-nosed LLJs in up to the 15% of the total number of measured profiles within a single night. Double-nosed LLJs have been also observed over southern China (Du et al. 2012; Du and Chen 2018, 2019a,b; Zhang and Meng 2019), where an LLJ below 1 km AGL coexisted with a synoptically driven LLJ within 1–3 km AGL, and in diurnal profiles over flat plains (Hoecker 1963) and coastal areas (Tuononen et al. 2017). In complex terrain, several studies have focused on the western United States finding double-nosed LLJs within the first 700–1000 m AGL (Banta et al. 2004; Savage et al. 2008), with the first nose close to the surface, at 50 m AGL according to Savage et al. (2008).

Existing literature has delved into the mechanisms that drive the LLJ formation within the PBL (e.g., Stull 1988; Stensrud 1996), with inertial oscillations being the most frequently observed under stable stratification, both in flat and complex terrains. Other mechanisms can be fronts and baroclinic weather patterns in flat terrain, orographic (wind splitting, ducting, or confluence around mountain barriers) and thermal effects (mountain and valley winds) in complex terrain. Few studies also delved into the mechanisms leading to a modification of the LLJ profile, but the formation of multiple noses was neither considered nor observed. For example, Sun et al. (2002) concluded that momentum transport associated with an intermittent-turbulence

Denotes content that is immediately available upon publication as open access.

Corresponding author: Francesco Barbano, francesco.barbano3@unibo.it

DOI: 10.1175/JAS-D-20-0274.1

© 2021 American Meteorological Society. For information regarding reuse of this content and general copyright information, consult the AMS Copyright Policy (www.ametsoc.org/PUBSReuseLicenses).

event altered the LLJ nose height. Similarly, [Viana et al. \(2009\)](#) observed a destructive interaction between the LLJ and a mesoscale buoyancy wave which was horizontally ducted and propagated in the opposite direction of the LLJ.

Conversely to LLJs, it appears that existing literature on double-nosed LLJs is limited and largely observational. No numerical or analytical studies of double-nosed LLJs have been reported so far, at least to our knowledge. Moreover, observational studies have not delved into the dynamics and formation mechanisms of double-nosed LLJs, but a few hypotheses have been suggested. Concerning the flat terrain, [Banta et al. \(2002\)](#) suggested (without validation) that each nose might be driven by inertial oscillations associated with horizontal pressure gradients at different spatial scales. [Du et al. \(2012\)](#) proposed that a synoptic forcing drove the upper nose formation at 1–3 km AGL above an LLJ driven by inertial oscillations below 1 km AGL. In the context of complex terrain, [Banta et al. \(2004\)](#) suggested that the intrusion of local drainage flows may force a secondary nose formation, although this hypothesis has not been further investigated.

The present study explores some of the open questions from the literature, and conducts a data analysis of recent double-nosed LLJ observations in complex terrain with the aim of improving our understanding of the double-nosed LLJ phenomenon and underlying driving mechanisms. The paper is structured as follows. [Section 2](#) describes the double-nosed LLJ driving mechanisms proposed in the current study. [Section 3](#) describes the measurement site, the equipment, and the data processing. It also defines the criteria to identify the double-nosed LLJs. [Section 4](#) is devoted to the discussion of the results. Finally, [section 5](#) draws the conclusions.

2. Double-nosed low-level jet driving mechanisms

As discussed in the following sections, nocturnal LLJs were frequently observed during quiescent nights (weak synoptic forcing) of the Mountain Terrain Atmospheric Modeling and Observations (MATERHORN) experiment ([Fernando et al. 2015](#)). These LLJs were typically confined in the lowest 100–150 m and persisting through the entire night. A peculiar feature of these LLJs was the formation of an additional nose which temporarily altered the canonical shape of the LLJ profile. Hereafter, we will refer to this transient nose as a secondary nose to differentiate it from the one which instead persisted throughout the night (called primary nose). On the basis of these observations, we propose two different mechanisms induced by boundary layer processes, that can drive the formation of a transient double-nosed LLJ in nocturnal (from sunset to sunrise) stably stratified flows in complex terrain. Necessary conditions to observe such double-nosed LLJs, and for the mechanisms to explain their formation are (i) the presence of a weak-synoptic forcing, (ii) the existence of an already-established LLJ, (iii) the occurrence of a local flow perturbation, and (iv) the development of a local wave capable of vertically transporting the flow momentum (required for one mechanism only).

Given this preamble, the proposed mechanisms are named 1) wind driven and 2) wave driven. The wind-driven mechanism

describes noses associated with different air masses simultaneously flowing one above the other from different directions. The double-nosed shape of the wind speed profile coincides with a sharp and pronounced variation of the wind direction between the primary and the secondary nose. Double-nosed LLJs traceable to this mechanism have already been observed in the literature (e.g., [Savage et al. 2008](#)). Conversely, the wave-driven mechanism has never been considered before. It assumes that the secondary-nose formation is driven by the vertical momentum transport carried by a wave, the latter being caused by an external flow perturbation. The occurrence of the secondary nose is always concomitant with wave activity and the wind direction describes a small and nearly constant rotation with the height within the PBL.

In this paper, we classify the observed double-nosed LLJs based on the change in wind direction with height into wave-driven and wind-driven cases, but we will only analyze the wave-driven cases in more detail. While the formation mechanism for the other cases is not discussed further, the wind-driven mechanism seems the most plausible hypothesis. In absence of synoptic forcing, no other mechanisms suggest a sharp wind turning rather than the intrusion of a local flow (i.e., our wind-driven mechanism). For example, the presence of waves in the PBL can induce a secondary nose but do not explain a sharp wind turning. Nevertheless, a robust verification of such a hypothesis would have required additional measurements and analyses beyond the scope of this investigation.

The wave-driven mechanism consists of four phases, namely, the preexistence of a canonical LLJ, wave generation, secondary-nose formation, and secondary-nose dissipation, each of them illustrated in [Fig. 1](#). As the LLJ grows during the night (preexistence of a canonical LLJ, [Fig. 1a](#)) a surface-flow perturbation (e.g., a downslope flow) suddenly and temporarily breaks the LLJ dynamics, generating a wave (wave generation, [Fig. 1b](#)). The vertical momentum transport associated with the wave subtracts momentum from the primary nose, carrying it to higher elevations where a secondary nose appears (secondary-nose formation, [Fig. 1c](#)). If the wave is dispersive, the secondary nose is transient and the conventional single-nosed shape is eventually restored (secondary-nose dissipation, [Fig. 1d](#)). Despite different waves may generate this mechanism, we discuss hereafter the case of inertial-gravity waves, particularly frequent in valleys and plains where they introduce a cross-wave component. This choice will then be tested in [section 4b](#), together with an assessment of the reliability of the wave-driven mechanism. The dispersion relationship of an inertial-gravity wave is

$$\omega^2 = \frac{k_z^2 f_c^2 + k_H^2 N^2}{k^2} = f_c^2 \sin^2 \phi + N^2 \cos^2 \phi, \quad (1)$$

where ω (s^{-1}) is the intrinsic frequency, f_c (s^{-1}) the Coriolis parameter, N (s^{-1}) the Brunt-Väisälä frequency, $k = \sqrt{k_H^2 + k_z^2}$ (rad m^{-1}) the total wavenumber with $k_H = k \cos \phi$ and $k_z = k \sin \phi$ (rad m^{-1}) being the horizontal and vertical wavenumber, respectively, and ϕ ($^\circ$) the propagation angle (i.e., the angle between the horizontal and the line of phase propagation;

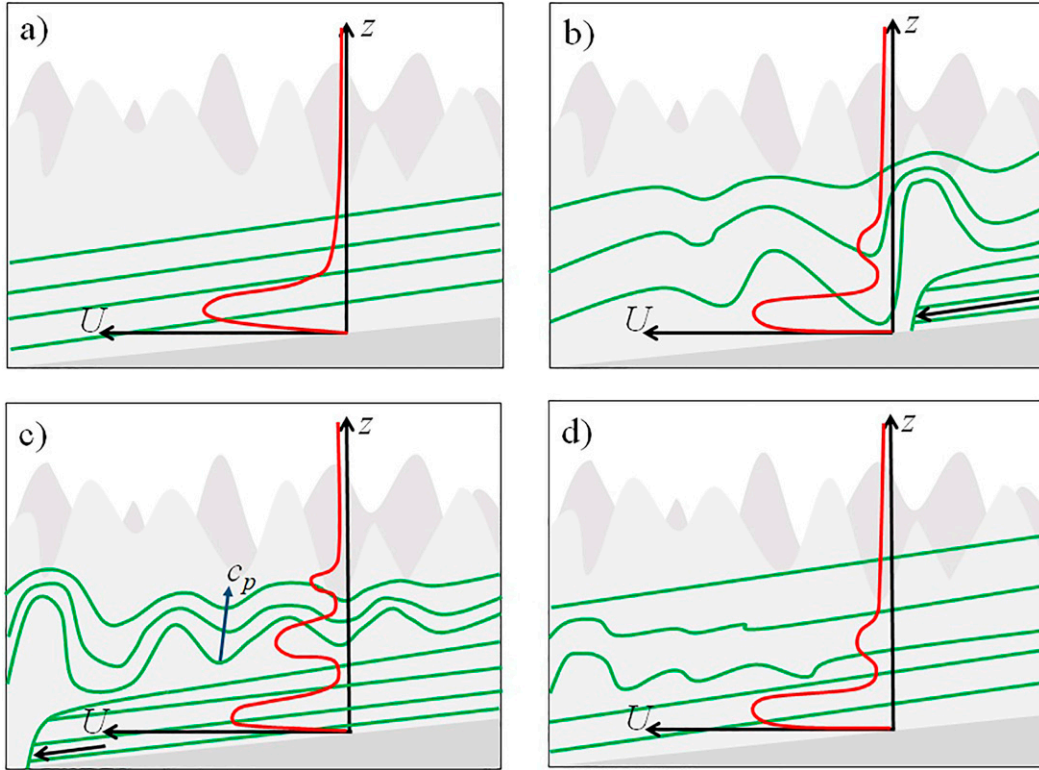


FIG. 1. Conceptual figure illustrating the wave-driven mechanism. (a) canonical LLJ, (b) wave generation, (c) secondary-nose formation, (d) secondary-nose dissipation. The green lines represent hypothetical streamlines of wind speed, the red lines the wind speed profile, the blue arrow the phase velocity of the wave, the gray triangles a generic sloping terrain, and the gray shading in the background the surrounding topography.

Gill 1982). Rearranging the rhs form of Eq. (1), the propagation angle ϕ is evaluated as

$$\phi = \cos^{-1} \sqrt{\frac{\omega^2 - f_c^2}{N^2 - f_c^2}}. \quad (2)$$

By evaluating the wave period T (s), the intrinsic frequency is computed through

$$\omega = \frac{2\pi}{T}. \quad (3)$$

Since inertial-gravity waves carry momentum along their phase direction, momentum transport will be predominantly vertical as ϕ approaches 90° . To verify if the momentum carried by the wave is sufficient to justify the secondary-nose formation, the momentum transport is evaluated with two methods, subsequently tested on specific cases of double-nosed LLJs in section 4b. Following Kim and Mahrt (1992), the inertial-gravity wave carries a vertical momentum M_w ($\text{kg m}^{-2} \text{s}^{-1}$) equal to

$$M_w(z) = \rho(z) \sqrt{\frac{[\overline{w\tilde{u}}(z), \overline{w\tilde{v}}(z)] \times [u(z), v(z)]}{U(z)}}, \quad (4)$$

where ρ (kg m^{-3}) is the air density, $\overline{w\tilde{u}}$ and $\overline{w\tilde{v}}$ ($\text{m}^2 \text{s}^{-2}$) the streamwise and cross-stream wave-momentum fluxes, u and v (m s^{-1}) the streamwise and cross-stream mean-wind velocity

components, and $U = \sqrt{u^2 + v^2}$ (m s^{-1}) the wind speed intensity. By integrating Eq. (4) in the appropriate layer with atmospheric depth $Z = z_t - z_b$ (m) and normalizing on Z itself, the mean wave momentum per meter $\langle M_w \rangle^{l,g}$ ($\text{kg m}^{-2} \text{s}^{-1}$) carried by the wave is

$$\langle M_w \rangle^{l,g} = \frac{1}{Z} \int_{z_b}^{z_t} M_w(z) dz, \quad (5)$$

where z_t and z_b are the top and bottom heights of the atmospheric depth Z where $\langle M_w \rangle^{l,g}$ is evaluated, and the superscripts l and g identify either a momentum loss or gain. The loss and gain values and their percentage ratio can be compared with a bulk momentum M_b ($\text{kg m}^{-2} \text{s}^{-1}$) estimated as

$$M_b(z, \delta t) = \rho_2(z, t_2)U(z, t_2) - \rho(z, t_1)U(z, t_1), \quad (6)$$

where δt (s) is the time difference between the time t_2 (s) of the double-nosed LLJ profile and the time t_1 (s) of the closest profile prior to the formation of the secondary maximum. Then the mean bulk-momentum loss and gain per meter $\langle M_b \rangle^{l,g}$ ($\text{kg m}^{-2} \text{s}^{-1}$) is obtained as the Z -normalized integral of Eq. (6) within the atmospheric depth $Z = z_t - z_b$ (m) involved in the momentum exchange:

$$\langle M_b \rangle^{l,g}(\delta t) = \frac{1}{Z} \int_{z_b}^{z_t} M_b(z, \delta t) dz. \quad (7)$$

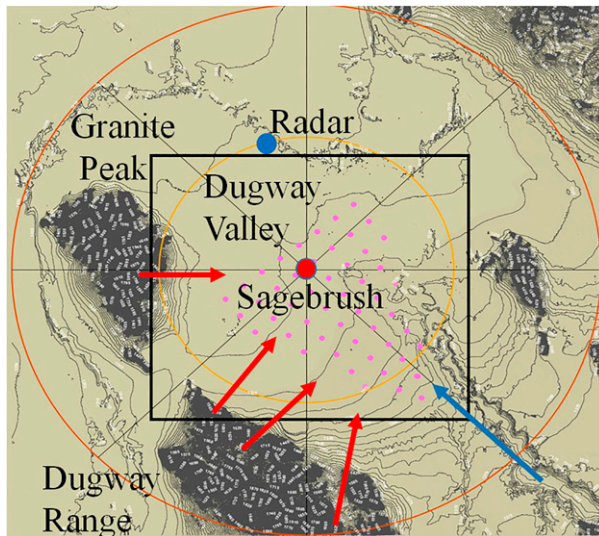


FIG. 2. Measurement site of the current study. The black rectangle indicates Dugway Valley, the red dot the Sagebrush site, the blue dot the radar, the pink dots the MINISAMS, the blue arrow the downvalley-flow direction (i.e., the direction of the main circulation within the valley), and the red arrows the direction of secondary flows that can perturb the downvalley flow. The circumferences show the distances from Sagebrush (10 km: yellow; 20 km: orange) the gray lines the cardinal points.

Although the rest of the discussion will focus on double-nosed LLJs observed in complex terrain, the conceptual framework here presented remains valid regardless of the specific site characteristics or investigated periods because the necessary conditions for this framework to be valid only involve weak-synoptic forcing, already-established LLJ, local flow perturbation, and generation of a wave, which are not site or period dependent. We can expect that the double-nosed LLJ characteristics (e.g., wind speeds and noses height) and occurrence probability/frequency can depend upon specific atmospheric conditions, seasonality, geographic position, local orography, and microclimate, but we do not expect these factors to modify the conceptual framework presented here. On the other hand, it is worth remarking that other mechanisms of double-nosed LLJ formation are in principle possible (e.g., Banta et al. 2002) and might be uncovered and/or verified by future studies.

3. Data collection and processing

a. Measurement site and equipment

To investigate the driving mechanisms of double-nosed LLJs in complex terrain, a suitable dataset has been extracted from the MATERHORN data repository (https://data.eol.ucar.edu/master_lists/generated/materhorn-x/). This dataset includes measurements collected over Dugway Valley (40.121 360°, -113.129 070°), Utah (marked with the black box in Fig. 2), where nocturnal LLJs were frequently observed during both fall (September–October 2012) and spring (May 2013) campaigns. Dugway Valley is approximately 30-km wide (from southwest to northeast) and 40-km long (from southeast to northwest). The valley floor

TABLE 1. Quiescent IOPs analyzed and respective operational period. The local time is MDT = UTC - 6 h.

		Operational period
Fall 2012	IOP0	2000 UTC 25 Sep–2000 UTC 26 Sep
	IOP1	2000 UTC 28 Sep–2000 UTC 29 Sep
	IOP2	2000 UTC 1 Oct–2000 UTC 2 Oct
	IOP6	0800 UTC 14 Oct–0800 UTC 15 Oct
	IOP8	1100 UTC 18 Oct–1800 UTC 19 Oct
Spring 2013	IOP4	2000 UTC 11 May–2000 UTC 12 May
	IOP7	2315 UTC 20 May–2000 UTC 21 May

is a gentle-sloping terrain (0.06°) at 1300 m above the mean sea level, characterized by arid soil and desert shrub. Dugway Valley is bounded by Granite Peak to the west (840 m AGL) and Dugway Range to the south (a mountain chain with a maximum altitude of 770 m AGL), the two of them separated by a 5-km gap.

In the present study, we analyze data collected during quiescent intensive observing periods (IOPs; listed in Table 1), characterized by wind speed at 700 hPa smaller than 5 m s^{-1} (Fernando et al. 2015). These quiescent IOPs are negligibly affected by synoptic forcing, aiding the development of a nocturnal stable boundary layer and the formation of a downvalley flow from southeast to northwest (blue arrow, Fig. 2) as the main circulation within Dugway Valley. This thermal circulation drives the early-evening development of the LLJ while being progressively superimposed by the inertial oscillations that regulate the subsequent nocturnal evolution of the LLJ up to the sunrise. This is argued in the complementary work by Barbano et al. (2021) where, after the initial growth of the nocturnal boundary layer, the observed LLJ evolution is indeed well reproduced by the analytical model of Van De Wiel et al. (2010), which calculates the horizontal wind field as inertial oscillations around the nocturnal equilibrium profile (represented by the Ekman spiral). However, complex terrain (unlike flat terrain) is intrinsically characterized by multiple flows interactions that perturb the main valley circulation. In our specific case, downslope flows from the surrounding mountains (red arrows, Fig. 2) may intrude the Dugway Valley and alter the LLJ circulation, by triggering the generation of waves that are able to redistribute momentum and energy, and modify the local atmospheric conditions (Sun et al. 2015b).

To analyze the LLJ vertical structure and detect the presence of multiple wind maxima, this study uses data collected from a DigiCORA tethered-balloon system (TTS111, Vaisala, Helsinki, Finland; Fernando 2017) deployed at the Sagebrush site (i.e., at the center of the valley, Fig. 2) during each IOP. This balloon allowed the retrieval of multiple vertical profiles of wind speed and direction, temperature, relative humidity, mixing ratio, and pressure (from which the height is derived using the hydrostatic equation) through an intensive sequence of ascents and descents during each IOP. Ascents of approximately 20 min were collecting data up to 400 m AGL with a vertical resolution of 1 m. Measurements collected

during balloon descents (lasting approximately 10 min) are discarded as affected by large uncertainties caused by the restoring mechanism of the balloon, bringing the instrumentation to the ground through an uneven and yanking path.

Each tethered-balloon ascent is preliminary checked to remove nonphysical values. Except for the wind direction, we use nonaveraged profiles to avoid losing information on the narrower noses oftentimes observed at the surface. This choice is motivated by the coherency of each tethered-balloon measurement with the height. In fact, each quantity has a smaller vertical variation than the respective instrumental uncertainty, which ensures that using nonaveraged data will not affect the double-nosed LLJ identification method defined in section 3b. Vertical averages are only used to deal with multiple measurements collected at the same height, caused by small vertical fluctuations (of order 1 m) of the balloon oftentimes observed at the takeoff from the ground. For the wind direction only, the 5-m mode was applied by counting the number of the wind-direction data belonging to each 10° bin the wind rose is divided into. Finally, no time average is applied (following Baas et al. 2009) as the tethered balloon already captures a sequence of snapshots of the mean state of the boundary layer.

Balloon measurements were complemented with ground-based observations to better characterize the near-surface valley circulation. These included data from the Surface Atmospheric Measurement Stations Mini Network (MINISAMS; Pace 2016), a permanent array of fifty-one 10-m towers evenly distributed within the valley area (pink dots, Fig. 2). Each tower is equipped with vane anemometers (05103, R. M. Young, Traverse City, Michigan) and temperature and relative-humidity probes (HMP45C-L, Campbell Scientific, Logan, Utah) at two vertical levels (2 and 10 m). Data from MINISAMS were stored at 1-min average, and further averaged over 5-min intervals to align with the flux-tower measurements. Nearby the balloon launching site (red dot, Fig. 2), a 20-m flux tower (Pace et al. 2017) was fully instrumented with three-axis sonic anemometers (CSAT3, Campbell Scientific) coupled with temperature and relative-humidity probes (HMP45C-L, Campbell Scientific) placed at five levels (0.5, 2, 5, 10, and 20 m) for continuous measurement of turbulent and mean meteorological variables. Temperature and relative-humidity data were sampled at 1 Hz, while sonic-anemometer data at 20 Hz. The flux-tower dataset is preliminary checked to detect and remove nonphysical values or instrumental failures. Following the method by Hojstrup (1993), a despiking procedure is applied over a 5-min data interval (Vickers and Mahrt 1997) to replace outliers with the nearest finite values in the time series. The despiked wind components are rotated to align the wind vector to the mean streamline direction (McMillen 1988) and then averaged on 5-min intervals. Selected subsets are averaged on smaller intervals to investigate specific processes.

To observe the possible occurrence of mesoscale-flow perturbations, data collected using a frequency-modulated continuous-wave (FMCW) radar (Pace 2017) were also analyzed. This radar was located 9 km to the north-northwest of Sagebrush site (blue dot, Fig. 2), and equipped with a bistatic parabolic antenna which allows collecting data up to 6 km AGL using a bandwidth

centered at 2.9 GHz. Data preprocessing involved the use of a phased-locked-loop digital frequency synthesizer to reduce the noise at 200 MHz.

b. Identification criteria for double-nosed low-level jets

Identification is the first key step in the analysis of the double-nosed LLJs. As done by many authors in the literature, the identification of LLJs with one or more speed maxima is performed using a criterion that compares the wind speed maxima and minima within a profile with absolute and relative thresholds. For example, Banta et al. (2002) identified the maxima using an absolute threshold. Baas et al. (2009) introduced a relative threshold because as the magnitude of a maximum grows, the absolute threshold will become as large as measurement fluctuations. Baas et al. (2009) also used an absolute threshold (equal to the instrumental uncertainty) to identify the minima. In this paper, we formulate a new criterion, refining those from Banta et al. (2002) and Baas et al. (2009), to better identify LLJs characterized by two noses. This newly proposed criterion couples the identification of maxima and minima, and reads as follows:

$$U_{\max} \geq \begin{cases} 1.5 \text{ m s}^{-1} + \max(U_{\min}^a, U_{\min}^b) & \text{for } U_{\max} < 7.5 \text{ m s}^{-1} \\ 1.25 \max(U_{\min}^a, U_{\min}^b) & \text{for } U_{\max} \geq 7.5 \text{ m s}^{-1}, \end{cases} \quad (8)$$

where

$$U_{\min}^i \leq \begin{cases} \min(U_g^a, U_g^b) - 0.5 \text{ m s}^{-1} & \text{for } U_{\min}^i < 2 \text{ m s}^{-1} \\ 0.8 \min(U_g^a, U_g^b) & \text{for } 2 \leq U_{\min}^i \leq 4 \text{ m s}^{-1} \\ \min(U_g^a, U_g^b) - 1.0 \text{ m s}^{-1} & \text{for } U_{\min}^i > 4 \text{ m s}^{-1}, \end{cases} \quad (9)$$

with Eq. (9) given for both $i = a$ and $i = b$. In Eq. (8) U_{\max} (m s^{-1}) indicates a wind speed maximum enclosed between the wind speed minima U_{\min} (m s^{-1}) below (superscript b) and above (superscript a) it. U_g (m s^{-1}) is the wind speed below (b) and above (a) each minimum measured at the height where the gradient dU/dz changes sign. This criterion requires an a priori guess of both wind speed minima and maxima, herein performed by a visual inspection of each nocturnal profile. First-guessed minima and maxima are then classified as wind speed minima and maxima of the profile if they fulfill Eqs. (8) and (9), respectively. Finally, a profile is classified as a double-nosed LLJ (as an LLJ) if two maxima (one maximum) satisfy Eq. (8). Although the proposed criterion is enunciated for double-nosed LLJs, it can be extended to identify LLJs with more than two noses.

Regarding maxima, we adopt the absolute threshold proposed by Banta et al. (2002) for $U_{\max} < 7.5 \text{ m s}^{-1}$, and the relative threshold by Baas et al. (2009) for $U_{\max} \geq 7.5 \text{ m s}^{-1}$. Regarding minima, we adopt a three-condition method. The threshold of 1.0 m s^{-1} proposed by Baas et al. (2009) is adopted for $U_{\min} > 4 \text{ m s}^{-1}$, while it is reduced to 0.5 m s^{-1} (according to our instrumental uncertainty) for $U_{\min} < 2 \text{ m s}^{-1}$. The relative threshold adopted in the range $2 \leq U_{\min} \leq 4 \text{ m s}^{-1}$ is obtained imposing a linear fit between the two previous conditions to guarantee that the minima identification in Eq. (9) follows a

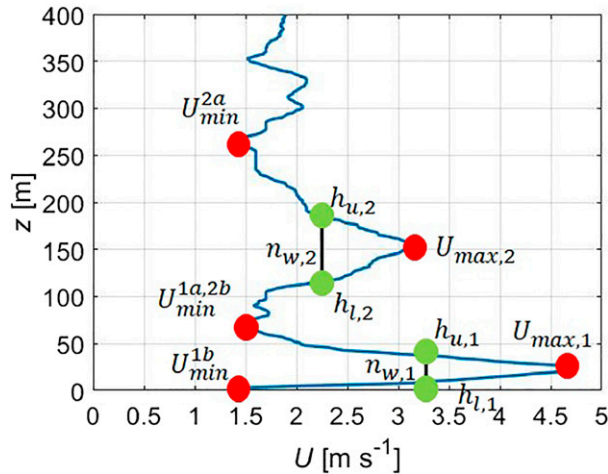


FIG. 3. Sketch of a double-nosed LLJ profile that reports the main variables used to characterize a nose: U_{\max} is the wind speed maximum, U_{\min} the wind speed minimum below (superscript b) and above (superscript a) it, and n_w the nose width defined as the difference between an upper height h_u and a lower one h_l , with 1 indicating the primary nose and 2 the secondary nose.

continuous piecewise function covering the whole range of wind speed.¹

To improve the characterization of the double-nosed LLJs, the nose width n_w is computed, treating each nose as two half-normal distributions extending from the wind speed maximum, respectively, to the upper and lower minima. The standard deviation σ_l (σ_u) (m s^{-1}) of the lower (upper) half-normal distribution enables to determine the lower (upper) height h_l (h_u) (m), defined as

$$h_l = z(U_{\max} - \sigma_l) \quad \text{for } z < z(U_{\max}), \quad (10)$$

$$h_u = z(U_{\max} + \sigma_u) \quad \text{for } z > z(U_{\max}), \quad (11)$$

and the nose width n_w

$$n_w = h_u - h_l, \quad (12)$$

according to Fig. 3. By delimiting the nose width, we can evaluate the wind-direction mode (and associated standard deviation) within each nose in the layer $h_l \leq z(U_{\max}) \leq h_u$, which difference is used for the determination of the driving mechanisms involved in the secondary-nose formation.

c. Wave-motion characterization

As key components of the wave-driven mechanism, physical characteristics of the inertial-gravity waves must be delineated

with precision, to investigate their role in the secondary-nose formation. The necessary accuracy is ensured by the high-frequency flux-tower measurements, enabling the observation of the wave generation driven by surface-flow perturbations and the wave propagation up to 20 m AGL.

Following Sun et al. (2015b), the inertial-gravity waves can be detected as periodic oscillations of the wind speed time series. For this analysis, we only use data from 5-, 10-, and 20-m levels, while discarding the 0.5- and 2-m ones due to the increasing turbulence mixing at the surface, according to Cava et al. (2015) and Sun et al. (2015a). The Brunt-Väisälä frequency N at the wave generation is estimated from the 5-min averaged potential temperature θ as

$$N = \sqrt{\frac{g}{\bar{\theta}} \frac{d\bar{\theta}}{dz}} \quad (13)$$

by averaging the datum obtained from Eq. (13) in the 5 min before, at, and after the wave generation (i.e., when the first crest/trough is observed). The reference potential temperature $\bar{\theta}$, is measured at 0.5 m, while the potential-temperature gradient $d\bar{\theta}/dz$ is computed using the discrete differences between two consecutive flux-tower levels. The wave period T is calculated from the wind speed time series as

$$T = \frac{1}{3} \sum_{z_s} \left(\frac{1}{n} \sum_{i=1}^n T_i \right), \quad (14)$$

where z_s identifies the 5-, 10-, and 20-m levels, n is the total number of time intervals t_i composed of single crest-trough couples observed in the wave signal, and $T_i = 2t_i$ is the period of each time interval. The 10-s averages are used in the calculation of T to detail each crest and trough of the wave. The intrinsic frequency ω is then calculated from T using Eq. (3). Both ω and N are then used to calculate the propagation angle ϕ with Eq. (2). Finally, the vertical phase velocity c_{pz} is evaluated from the 10-s-averaged wind speed. This averaging time was chosen to capture the variations in the measurements between flux-tower levels. We estimate c_{pz} as the ratio between the distance in height of two consecutive levels and the delay of the wave phase (i.e., the delay between the first wave crest/trough at two consecutive flux-tower levels). The errors associated with the wave period are calculated as the standard deviation of T ; for the other quantities, we follow the error-propagation theory (Taylor 1997).

4. Results and discussion

a. Double-nosed low-level jet classification

Among the 94 nocturnal profiles measured with the tethered balloon, 78 (the 83%) fulfill the criterion in Eqs. (8) and (9): 58 LLJs are single nosed (the 62% of the total number of nocturnal profiles) while 20 are double-nosed LLJs (the 21%). These percentages are in line with Pichugina et al. (2007), where canonical and double-nosed LLJs were observed in the 70% and 15% of the total number of profiles, respectively. The 20 double-nosed LLJs are unevenly distributed among the IOPs (see

¹ From an operational perspective, if Eq. (9) fails, we identify the minima in a (single-nosed) LLJ profile by visual inspection following simple rules: 1) below the nose, we impose $U_{\min} = 0 \text{ m s}^{-1}$, and 2) above the nose, U_{\min} is assigned as the smallest wind speed measured above it. In the contingency of a double-nosed LLJ profile, the previous rules are integrated with the following: 3) between two noses, U_{\min} is assigned as the smallest wind speed between them, and 4) above the second nose, U_{\min} is assigned as the smallest wind speed measured above it.

TABLE 2. Double-nosed LLJ profiles identified in MATERHORN data during quiescent nights. The detection time and period corresponds to the sounding takeoff time if the double-nosed LLJ is observed in a single profile. The detection time and period corresponds to the takeoff times of the first and last soundings enclosing the observation period if the double-nosed LLJs are observed in consecutive profiles. No. is the total number of consecutive ascents that shows the same double-nosed LLJ event; Φ_1 and Φ_2 are the mode and associated standard deviations of wind direction within the primary and secondary noses, respectively, as delimited by $h_{l,i}$ and $h_{u,i}$ ($i = 1, 2$) defined in Eqs. (10) and (11); $|\Delta\Phi| = |\Phi_2 - \Phi_1|$ is the wind direction difference between the noses and associated error. Double-nosed LLJs associated with cases A, B, and C are classified as wave driven.

		Detection time and period	No.	Φ_1 (°)	Φ_2 (°)	$ \Delta\Phi $ (°)	Case
2012 Fall	IOP0	0913–1016 UTC 26 Sep	3	140 ± 5	228 ± 8	88 ± 13	
	IOP0	1049–1224 UTC 26 Sep	4	70 ± 1	347 ± 7	83 ± 8	
	IOP1	0514 UTC 29 Sep	1	154 ± 5	107 ± 4	47 ± 9	
	IOP1	0717 UTC 29 Sep	1	142 ± 1	220 ± 3	78 ± 4	
	IOP1	1045–1117 UTC 29 Sep	2	128 ± 9	233 ± 12	105 ± 21	
	IOP1	1218 UTC 29 Sep	1	160 ± 4	244 ± 6	84 ± 10	
	IOP2	1231 UTC 2 Oct	1	219 ± 6	171 ± 3	48 ± 9	
	IOP8	0515 UTC 19 Oct	1	104 ± 3	96 ± 4	8 ± 7	B
	IOP8	0909–1013 UTC 19 Oct	3	125 ± 4	131 ± 8	6 ± 12	C
2013 Spring	IOP4	0552–0626 UTC 12 May	2	131 ± 4	220 ± 4	89 ± 8	
	IOP4	0932 UTC 12 May	1	147 ± 10	159 ± 4	12 ± 14	A

Table 2). In each double-nosed LLJ, the secondary nose is above the primary one. The primary-nose maximum is between 10 and 150 m AGL, while the secondary-nose one is between 90 and 340 m AGL. Overall, the wind speed maximum of the primary nose follows a Gaussian distribution within the range 2.9–7.0 m s⁻¹; in 15 cases, the wind direction is in the range 90° ≤ Φ ≤ 180°. The nose width oscillates in the range 6 ≤ n_w ≤ 77 m. The secondary-nose variability is typically larger than the primary one. The wind speed maxima are in the range 3.1–9.3 m s⁻¹, following a Gaussian distribution skewed toward the smallest edge. For this reason, the secondary-nose maxima can be either larger (observed 9 times) or smaller (11 times) than the primary one. The wind direction also shows a larger variety, being 9 times in the range 180° ≤ Φ ≤ 270°, 7 within 90° ≤ Φ ≤ 180°. Finally, the nose width oscillates in the range 21 ≤ n_w ≤ 177 m.

Among the observed double-nosed LLJs, 15 profiles are classified as wind driven and 5 as wave driven, considering the wind-direction difference between primary and secondary noses as a sole discriminant. As defined in section 2, the wave-driven double-nosed LLJs are characterized by a small and nearly constant rotation of the wind direction with the height. The result is a secondary nose directed approximately as the primary one, as highlighted in Table 2 where the values of |ΔΦ| are always smaller than the associated errors during the wave-driven events. Conversely, the wind-driven double-nosed LLJs show values of |ΔΦ| of at least 47°, but typically above 80°. An example of double-nosed LLJ identified as wind driven is given in Fig. 4. The sharp and sudden wind-direction variation (88°) creates a discontinuity at the base of the secondary nose, providing a modification in the LLJ dynamics. Compared to the primary nose, the secondary one shows similar wind speed maximum and potential-temperature gradient evolving into isothermal conditions in the atmosphere above the nose. These observations support the hypothesis of an upper-airflow intrusion while excluding wave/turbulence activity and expected rotations with the height (e.g., the Ekman spiral) as driving mechanisms. Nevertheless, additional upper-air measurements

and analyses would be required to investigate this secondary flow in the surrounding of the tethered-balloon site, leaving the wind driven as a plausible suggestion.

Concerning the wave-driven profiles, three events have been observed: case A during IOP4, cases B and C within IOP8. Both cases A and B show a single double-nosed LLJ profile, named A-2 and B-2, respectively. During case C, three double-nosed LLJ profiles are consecutively measured, namely, C-2_a, C-2_b, and C-3. We adopt a unique nomenclature for the first two double-nosed LLJs of case C because they share similar flow characteristics. Figures 5 and 6 show the evolution of wind speed, wind-direction, and potential-temperature profiles for each wave-driven double-nosed LLJ from immediately before its occurrence (A-1, B-1, and C-1) to its dissipation (A-3, B-3, and C-4) in which the unperturbed LLJ is restored. Table 3 lists the main characteristics of the wave-driven double-nosed LLJs. During cases A and B, the dissipation is observed after approximately 30 min. During case C, primary and secondary noses move above 100 and 300 m AGL, respectively, passing from condition C-2_b to C-3. Then the secondary-nose dissipation is observed in C-4, after approximately 90 min. The different duration of these events could be related to the different perturbations that trigger the double-nosed LLJs formation. While cases A and B will be associated with a surface perturbation (section 4c), C may be linked with a mesoscale flow and a downward wave-momentum transport from it as supported by the secondary-nose characteristics in both C-2_a and C-2_b. Differently from A-2 and B-2, the secondary-nose maximum is approximately 35% larger than the primary one. However, given the limited vertical extension of the tethered-balloon profiles (400 m), the hypothesis of a mesoscale perturbation as triggering mechanism will only be qualitatively investigated in section 4c.

b. Wave-driven mechanism verification

The following analysis is focused on the corroboration of the wave-driven mechanism suggested in section 2. Specifically, cases

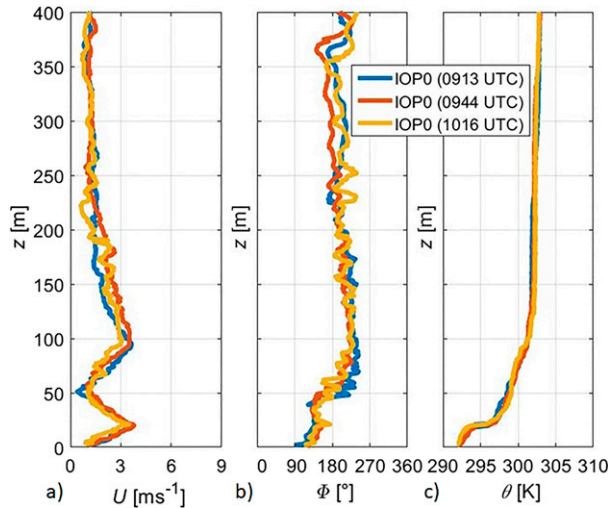


FIG. 4. Example of (a) wind speed, (b) wind direction, and (c) potential-temperature profiles during the first wind-driven double-nosed LLJ event observed within the IOP0 (0913–1016 UTC).

A and B are analyzed to prove that an inertial-gravity wave can drive the secondary-nose formation by means of momentum transported from the primary nose.

In both cases, the appearance of the double-nosed LLJ is preceded by a reduction-shift perturbation composed of a wind speed reduction and a wind-direction shift. The first occurs at all the tower levels (Figs. 7a,c), and the second decreases with the height almost disappearing at 20 m AGL (Figs. 7b,d), suggesting that the flow perturbation is confined at the surface and cannot generate or directly contribute to the formation of the secondary nose. At the same time, this reduction-shift perturbation induces a wavelike motion (Fig. 7) that is associated with an inertial-gravity wave. Note that no significant turbulent activity is detected at this stage; thus the double-nosed LLJs formation is not driven by intermittent-turbulence events at the surface. The wave physical parameters are computed according to section 3c and listed in Table 4. The inertial-gravity waves observed during cases A and B have similar vertical phase velocity c_{pz} , period T , and intrinsic frequency ω , in line with typical values at midlatitude (Holton 2004). The hypothesis of predominant vertical momentum transport is ensured for all three cases by the propagation angle ϕ . Despite ϕ is close to 90° , ω is buoyancy-dominated, as the buoyancy term $N^2 \cos^2 \phi$ and inertial term $f_c^2 \sin^2 \phi$ in Eq. (1) assume values of order 10^{-5} and $10^{-8} \text{ rad}^2 \text{ s}^{-2}$, respectively.

The delay time dt between the concomitant observation of the perturbation-wave generation and the double-nosed LLJ observation ensures the wave has enough time to cover the distance between the ground and the secondary-nose layer. Note that this delay time is calculated considering the instant when the tethered balloon reaches the secondary-nose layer, thus adding few minutes (the exact amounts depend on the case) to the sounding time (i.e., the takeoff

time). During case A, we start observing the effects of the perturbation-wave generation at Sagebrush site at 0911 UTC (Figs. 7a,b). The observation of the secondary nose in A-2 (occurring at 0938 UTC) is therefore delayed by $dt = 27$ min. During case B, the reduction-shift perturbation lasts 30 min from 0432 to 0502 UTC (possibly caused by the larger values of N with respect to case A), when the wave is generated (Figs. 7c,d). In this second case, the observation of the secondary nose in B-2 occurs at 0522 UTC, with a delay $dt = 20$ min from the wave generation. Considering the vertical phase velocity, the waves need $dt_{pz} = 10$ and 12 min, respectively, in cases A and B to move from the surface to the secondary-noses height. Since the delay times dt are larger than the wave propagation times dt_{pz} , the waves have enough time to subtract momentum from the primary noses and carry it to the atmospheric layer of the secondary ones.

To verify that the momentum carried by the wave is sufficient to justify the formation of a secondary nose, the methods proposed in section 2 are applied to cases A and B, comparing the wave momentum transported by the inertial-gravity wave with the observed bulk-momentum variation at the secondary nose occurrence. As determined in Eq. (4), the computation of the wave momentum relies on the evaluation of the wave kinematic momentum fluxes $\overline{w'u}$ and $\overline{w'v}$, which in turn require the estimation of the vertical velocity component w , a variable not directly measured by the tethered-balloon instrumentation. From the good overall agreement between balloon and sonic-anemometers measurements, an approximated vertical velocity component for each tethered-balloon profile is estimated by using an empirical relationship between w and the horizontal wind speed retrieved from the sonic-anemometers measurements (see the appendix). Although the measurement comparison is limited to the first 20 m AGL and the estimation of w can only be an approximation, the good match between the approximated and measured values of w suggests the empirical relationship is our best solution to estimate w along the tethered-balloon profile. Alongside the horizontal velocity components, this approximated w is then linearly interpolated in time to obtain a regular array of data. From that, the kinematic wave-momentum fluxes are calculated by integrating the spectral covariances $wu(z, f)$ and $wv(z, f)$. The covariances are computed from the fast Fourier transform on the Hamming window in which the waves were observed, at each level z of the tethered-balloon sounding and over the frequency range f where the wave is active. The frequency range is retrieved from the dispersion relationship in Eq. (1) as the interval $f_c - N$, and it is further restricted to $f_0 - N$ to avoid superposition between the wave motion and the mean flow. Note that the largest eddy frequency $f_0 = \epsilon / \text{rms}(U)^2$ is obtained from sonic-anemometer measurements of the energy dissipation rate ϵ and $\text{rms}(U)$ averaged among the whole nocturnal period and the vertical depth of the flux tower. By inserting the kinematic wave-momentum fluxes in Eq. (4), the wave momentum is evaluated and compared with the bulk momentum in Figs. 8a and 8b for cases A and B, respectively. For case A, two well-defined layers are evident in the first 250 m (Fig. 8a), respectively characterized by a mean momentum loss $\langle M_w \rangle^l \approx -1.44 \text{ kg m}^{-2} \text{ s}^{-1}$ between 0 and 100 m and a mean momentum gain $\langle M_w \rangle^g \approx 0.82 \text{ kg m}^{-2} \text{ s}^{-1}$ between

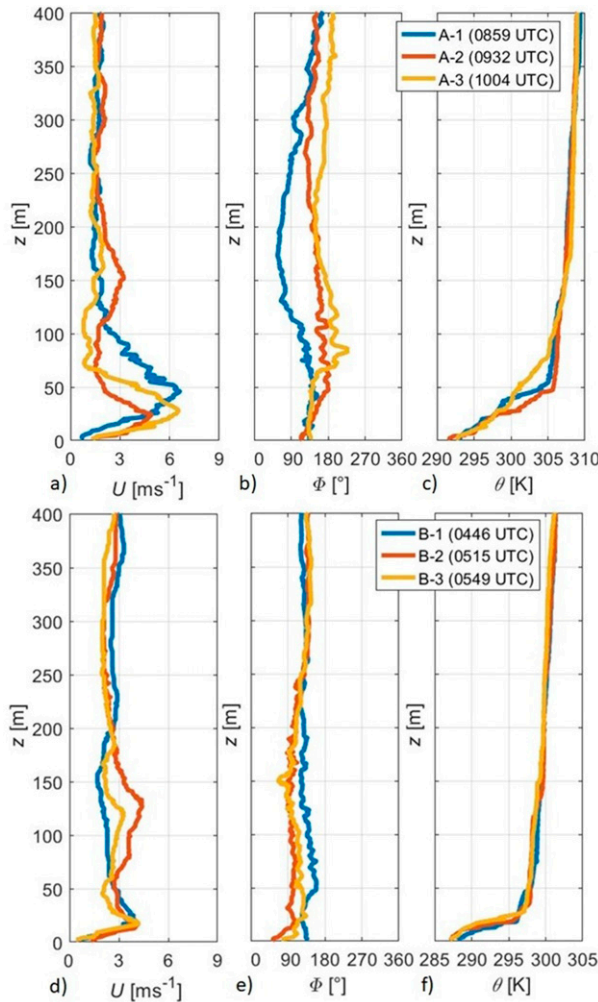


FIG. 5. Evolution of the wind speed, wind-direction, and potential-temperature profiles before and after (a)–(c) case A and (d)–(f) case B.

100 and 250 m, both computed using Eq. (5). These values give a percentage gain-to-loss ratio of the 57%, accounting for the momentum transported by the inertial-gravity wave from the surface layer (0–100 m) to the one above (100–250 m). The remaining 43% may be dissipated by the wave, straightening the condition of having a dispersive wave as a momentum carrier. The bulk momentum is estimated using Eq. (6), subtracting the momentum in A-2 from that in A-1. This is considered a bulk estimation because there is always a 30-min gap between consecutive profiles and because the perfect profile to compare the double-nosed LLJ with would have been at 0911 UTC, corresponding to the wave generation. Following the same procedure adopted for the wave-momentum gain and loss estimations, Eq. (7) gives a mean bulk-momentum loss $\langle M_b \rangle^l \approx -2.01 \text{ kg m}^{-2} \text{ s}^{-1}$ between 0 and 100 m, and a gain $\langle M_b \rangle^g \approx 1.21 \text{ kg m}^{-2} \text{ s}^{-1}$ between 100 and 250 m, corresponding to a momentum gain-to-loss ratio of the 60%. Both momentum gain and loss absolute values

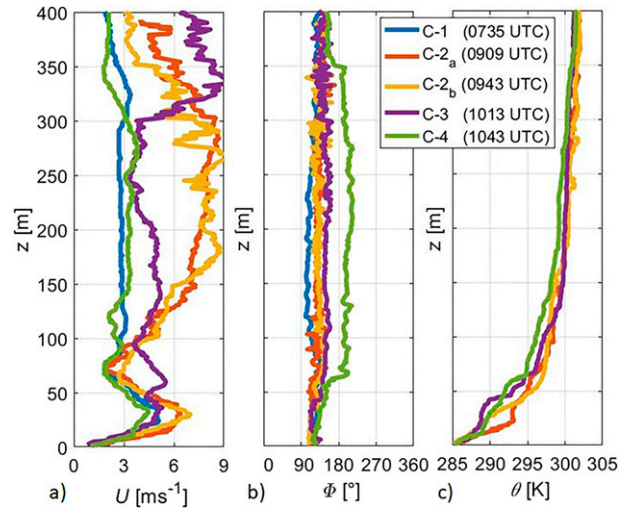


FIG. 6. Evolution of the (a) wind speed, (b) wind direction, and (c) potential-temperature profiles before and after case C.

and percentage exchanges find a very good agreement between the two evaluation methods. This agreement corroborates the initial hypothesis, confirming the double-nosed LLJ is generated by the momentum transport of an inertial-gravity wave from the surface ($z < 100 \text{ m}$) to the layer above ($100 < z < 250 \text{ m}$). A supplementary confirmation is also provided by case B among which the same comparison is performed with similar results (Fig. 8b). Here, the mean wave-momentum loss $\langle M_w \rangle^l \approx -0.59 \text{ kg m}^{-2} \text{ s}^{-1}$ between 0 and 65 m and gain $\langle M_w \rangle^g \approx 0.47 \text{ kg m}^{-2} \text{ s}^{-1}$ between 65 and 190 m gives a ratio of the 79%. Similarly, the bulk momentum is calculated by subtracting the momentum in B-2 from that in B-1. The result is a mean bulk-momentum loss $\langle M_b \rangle^l \approx -0.88 \text{ kg m}^{-2} \text{ s}^{-1}$ between 0 and 65 m and a gain $\langle M_b \rangle^g \approx 0.79 \text{ kg m}^{-2} \text{ s}^{-1}$ between 65 and 190 m, giving a ratio of 90%. Compared to case A, the momentum transported is smaller as smaller is the secondary-nose momentum. Conversely, the momentum-transport efficacy is larger in case B, maybe due to the smaller atmospheric depth where the double-nosed LLJ has developed. Nevertheless, this difference may be due to the uncertainties associated with the computation.

A wave motion is also detected during case C using sonic-anemometer data (Fig. 7c). As reported in Table 4, this wave is characterized by a larger period than cases A and B, and by a negative vertical phase velocity, accounting for downward momentum propagation. As hypothesized in section 4a, this downward propagation may be a symptom of the wave-driven mechanism triggered by a mesoscale perturbation at higher elevations. However, there is no evidence that the surface wave and the mesoscale perturbation are correlated, leaving again case C as a suggestion.

c. Flow perturbation

As hypothesized in section 2 the generation of the inertial-gravity wave is caused by a flow perturbation. In this section, we explore different perturbations as possible causes of

TABLE 3. Wave-driven double-nosed LLJ characterization by the estimation of wind speed maximum U_{\max} , height of wind speed maximum h_{\max} , wind direction Φ , and nose width n_w for both noses. The last row reports the wind direction difference $\Delta\Phi$ between the noses. The reported time is the sampling period in which each profile is detected by tethered balloon in Sagebrush.

		Time (UTC)				
		0932–0948 (A-2)	0515–0540 (B-2)	0909–0928 (C-2 _a)	0943–1003 (C-2 _b)	1013–1033 (C-3)
Primary nose	U_{\max} (m s ⁻¹)	4.9	4.2	6.4	7.0	5.2
	h_{\max} (m)	24	18	30	30	144
	Φ (°)	147	104	114	113	148
	n_w (m)	21	6	33	21	77
Secondary nose	U_{\max} (m s ⁻¹)	3.3	4.5	8.7	9.3	9.7
	h_{\max} (m)	152	131	284	268	335
	Φ (°)	159	96	128	127	139
	n_w (m)	40	32	177	137	23
	$ \Delta\Phi $ (°)	12	8	14	14	8

wave generation. As measured from the MINISAMS network, the wind-velocity field at 2 m shows that the flow perturbation occurs at the surface as a shallow downslope flow intruding the valley from Dugway Range (case A) and Granite Peak (case B), altering the previously unperturbed valley circulation (Figs. 9a and 10a). At the onset of the perturbation of case A, a bending of the wind direction starts at

0855 UTC, turning the wind vectors from southeast to southwest in the proximity of Dugway Range (Fig. 9b). The downslope flow propagates northward to the valley center, involving Sagebrush at 0910 UTC (Fig. 9c). After 20 min from the perturbation onset, the downvalley direction is restored in Sagebrush at 0915 UTC (Fig. 9d). A small temperature decrease ($\Delta\theta \approx 0.5$ K) is observed during the intrusion (Fig. 9c), suggesting the downslope flow has

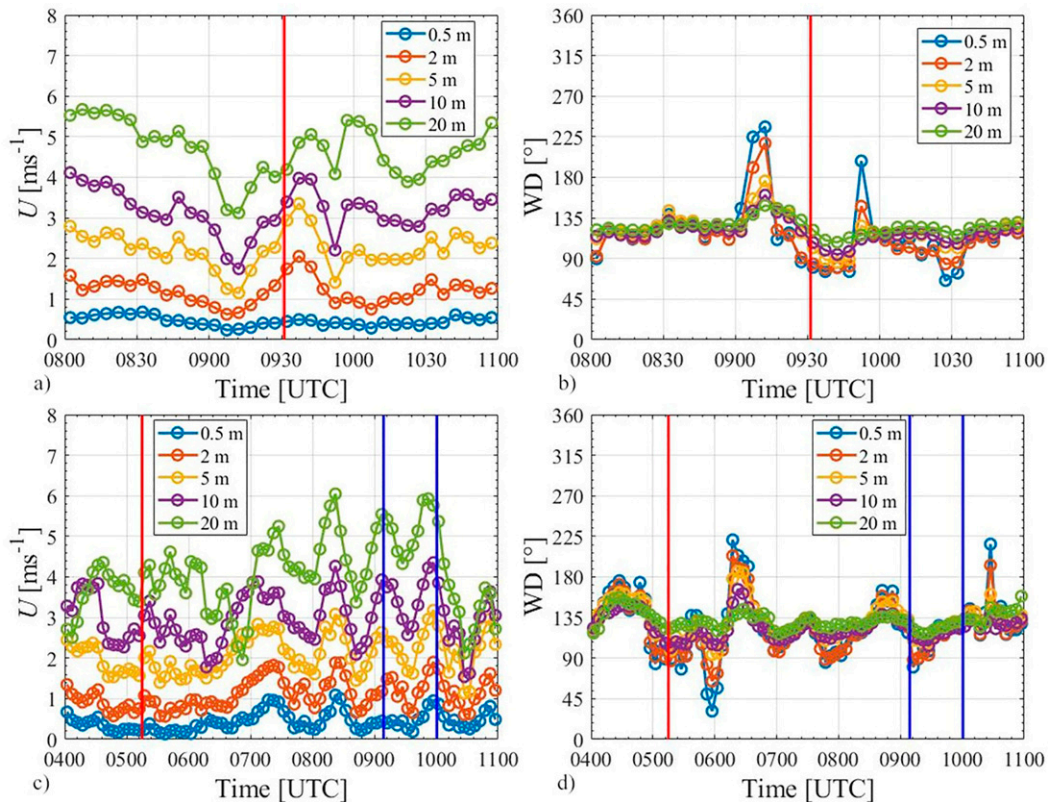


FIG. 7. The 5-min-average time series obtained from flux-tower measurements of the (left) wind speed and (right) wind direction before and after (a), (b) case A and (c), (d) cases B and C. The red line indicates the time in which the tethered balloon starts to measure A-2 in (a) and (b), B-2 in (c) and (d). The blue lines in (c) and (d) indicate the time interval in which the tethered balloon measures C-2.

TABLE 4. Inertial–gravity wave characterization by flux-tower data at 5, 10, and 20 m. N is the Brunt–Väisälä frequency during the wave generation, T the period, ω the intrinsic frequency, c_{pz} the vertical phase velocity, and ϕ the propagation angle.

	Case A	Case B	Case C
N (s^{-1})	$(8.4 \pm 0.6) \times 10^{-2}$	$(11.4 \pm 0.4) \times 10^{-2}$	$(7.7 \pm 0.6) \times 10^{-2}$
T (s)	1000 \pm 100	1300 \pm 400	2700 \pm 300
ω ($rad\ s^{-1}$)	$(6.0 \pm 0.6) \times 10^{-3}$	$(5 \pm 2) \times 10^{-3}$	$(2.3 \pm 0.3) \times 10^{-3}$
c_{pz} ($m\ s^{-1}$)	$(2.5 \pm 0.6) \times 10^{-1}$	$(1.7 \pm 0.6) \times 10^{-1}$	$(-2.0 \pm 0.4) \times 10^{-1}$
ϕ ($^\circ$)	85.88 \pm 0.01	87.51 \pm 0.02	88.29 \pm 0.01

similar temperatures to the surface unperturbed circulation in the valley.

Case B shows a similar evolution. The wind vectors start bending northeastward in the proximity of the southern end of Granite Peak at 0430 UTC (Fig. 10b). The perturbation propagates toward northeast (Fig. 10c) involving Sagebrush at 0445 UTC and ceases at 0455 UTC (Fig. 10d), after 25 min from its onset. During case B, the air-temperature decrease ($\Delta\theta \approx 1.5\text{ K}$) involves the entire Dugway Valley.

Since the MINISAMS did not retrieve a surface-flow perturbation before case C, the origin of this perturbation is probably not local nor surface driven. In this case, the formation of the double-nosed LLJ may be induced by a mesoscale-flow perturbation, as suggested by the backscatter signal measured by the radar, showing an oscillatory motion around 1400 m from 0810 UTC (Fig. 11). This perturbation starts propagating downward at 0850 UTC, possibly inducing the flow oscillation reported at 600 m between 0915 and 0930 UTC. This flow oscillation fits with the first observation of the double-nosed LLJ in C-2_a, providing a suggestion for the wave generation. Moreover, it would also explain the large intensity of the secondary noses as they would directly scale with the mesoscale flow. However, the evidence provided by radar data is not sufficient to evaluate the characteristics of the wave. Supplementary data would have been necessary to detail the mesoscale flow to verify the downward momentum transport as the driven mechanism of the double-nosed LLJ during case C.

5. Conclusions

This paper presented an in-depth observational analysis of double-nosed LLJs developing within the PBL, where a transient wind speed nose (secondary nose) appears above the LLJ maximum (primary nose). The analysis is carried out using the comprehensive dataset collected during the first two MATERHORN field experimental campaigns carried out in Dugway Valley, Utah, in autumn 2012 and late spring 2013. Two different mechanisms have been presented as responsible for the formation of nocturnal double-nosed LLJs, namely, wind-driven and wave-driven mechanisms. In the wind driven, the secondary nose is systematically associated with a sharp, large variation in wind direction, driven by a flow intrusion above the primary nose. In the wave driven, a nearly constant wind direction is maintained between the two noses, with the secondary one driven by the vertical momentum transport associated with a wave, the latter generated by a flow perturbation. This paper has

attempted to the formalization and verification of the wave-driven mechanism.

A total of 20 nocturnal double-nosed LLJ profiles have been identified during quiescent periods and upon a careful redefinition of the LLJ identification criteria. Five of them have been classified as wave driven. During two of these events, the flow perturbation occurred at the surface as a downslope flow intruding the main circulation within the valley

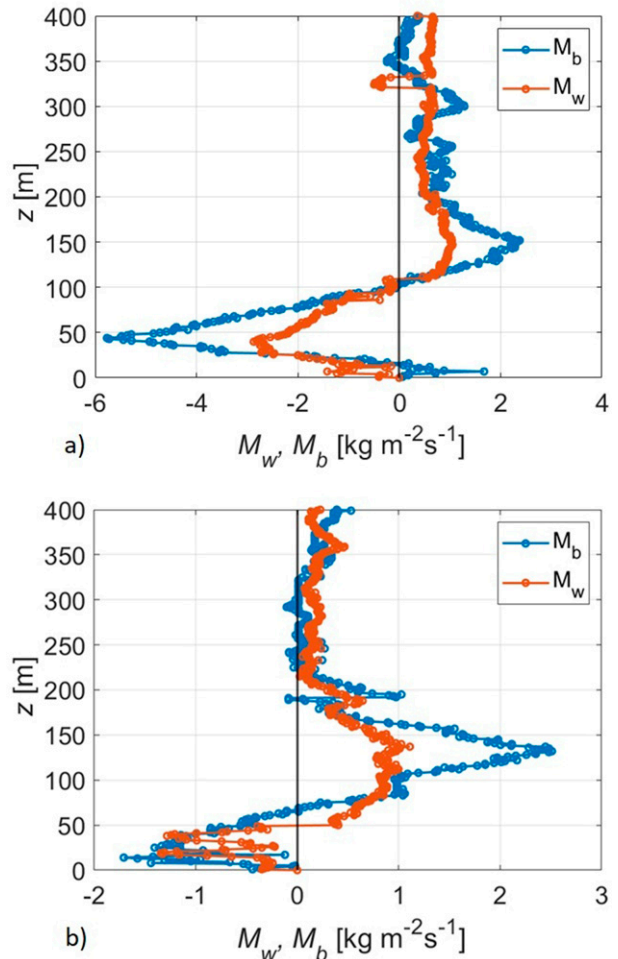


FIG. 8. Bulk M_b (blue) and wave M_w (red) momentum profiles for (a) case A and (b) case B, as computed using Eqs. (6) and (4), respectively.

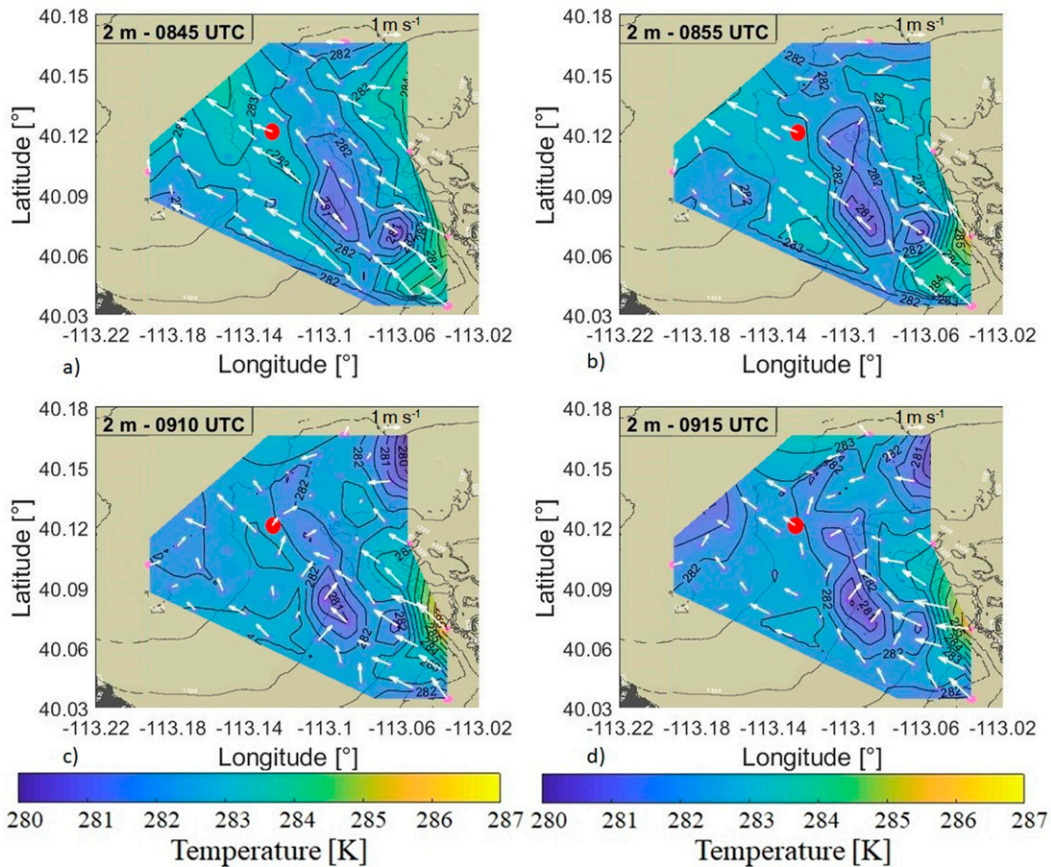


FIG. 9. Evolution of the temperature and wind speed fields at 2 m in Dugway Valley during case A. The fields are retrieved from the MINISAMS data averaged over 5 min. The white arrows start from MINISAMS position. The red dot indicates the position of the Sagebrush site.

from the surrounding slopes. From these flow collisions, an inertial-gravity wave is generated, breaking the already-established LLJ dynamics and transporting momentum from the primary nose to a higher elevation where the secondary nose is observed. The canonical (single-nosed) shape of the LLJ is then restored after the dissipation of the secondary nose.

Further field studies could be encouraged to improve our knowledge of the double-nosed LLJs driving mechanisms. Additional observations are required to provide a robust verification and generalization of the two mechanisms proposed in the current study, especially of the wind-driven mechanism which is only hypothesized. Reinterpretation of past studies in this context may also be of use. From the pure process perspective, further studies may reveal different causes of the wave generation in the wave-driven mechanism (starting from the suggestion on the submesoscale perturbation given in the current investigation), and provide an exhaustive interpretation for the dissipation process of the secondary nose.

Acknowledgments. The research was partially funded by the Office of Naval Research Award N00014-11-1-0709, Mountain Terrain Atmospheric Modeling and Observations (MATERHORN) Program.

Data availability statement. The dataset analyzed during the current study is available in the EOL data archive (<https://data.eol.ucar.edu>). This dataset was derived from the following public domain resource: MATERHORN data, https://data.eol.ucar.edu/master_lists/generated/materhorn-x.

APPENDIX

Estimation Method for the Vertical Velocity Component

The vertical velocity component w for the tethered-balloon profiles is estimated using an empirical relation retrieved from sonic anemometers. The good agreement between balloon (superscript B) and sonic anemometers (superscript S) measurements of the horizontal wind components (u, v) shown in Fig. A1 suggests the vertical components should behave likewise. Therefore, we use the sonic anemometers data to compute the angle

$$\psi^S = \tan^{-1} \frac{w^S}{U_h^S}, \quad (\text{A1})$$

with $U_h^S = [(u^S)^2 + (v^S)^2]^{1/2}$ the horizontal wind speed. ψ^S is used within the double-rotation procedure to align the wind

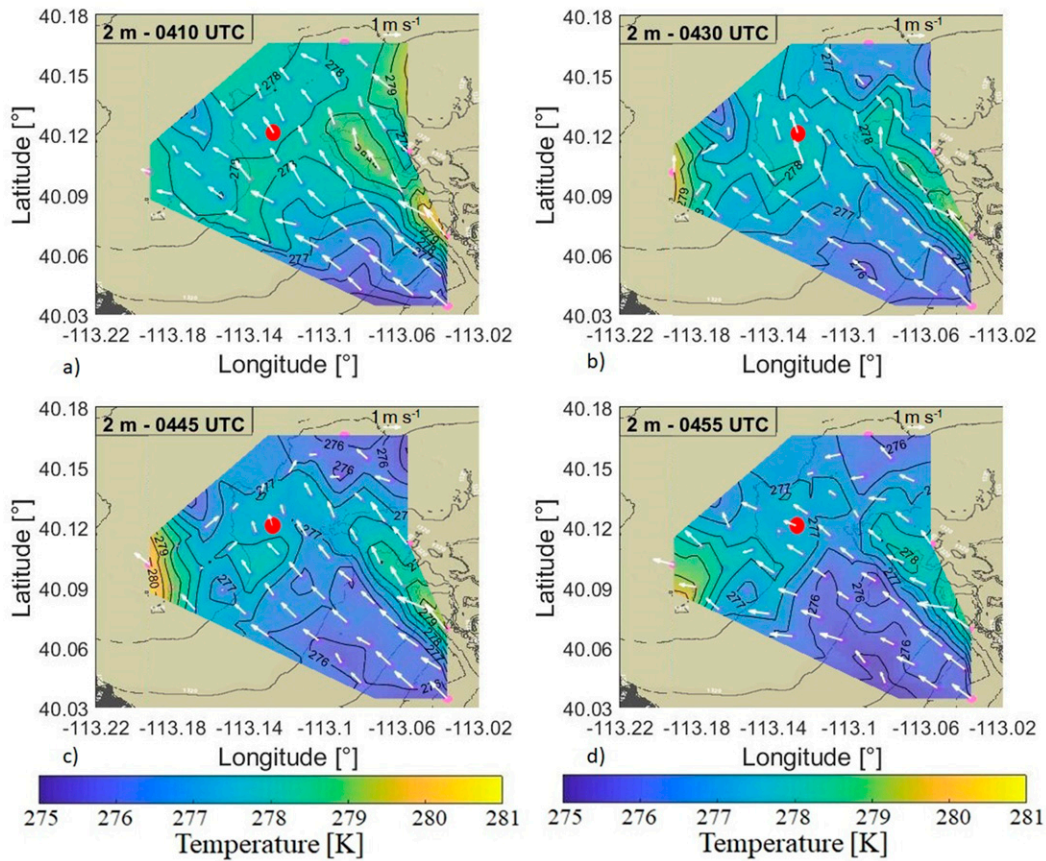


FIG. 10. Evolution of the temperature and wind speed fields at 2 m in Dugway Valley during case B. The fields are retrieved from the MINISAMS data averaged over 5 min. The white arrows start from MINISAMS position. The red dot indicates the position of the Sagebrush site.

vector to the streamline direction (McMillen 1988) and is approximately equal to the terrain slope. Given Eq. (A1), ψ^S is inspected as a function of U_h^B at the four upper levels of the flux tower, showing a bimodal behavior (see Fig. A2a). For small

wind speed, U_h^B (i.e., the wind speed measured by the tethered balloon) is constant with ψ^S , while above a certain threshold (equal to 2 m s^{-1} from visual inspection) the dependency becomes linear. U_h^B values below the threshold are

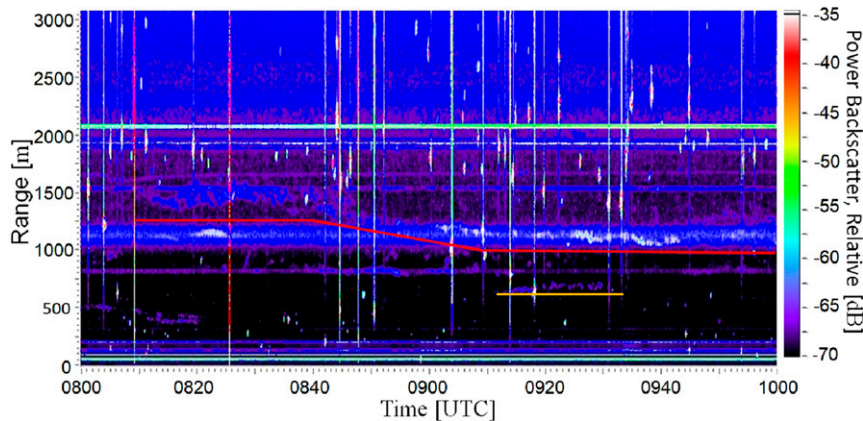


FIG. 11. Continuous time–height display of the returned-signal-relative amplitude measured by the FMCW radar before and during case C. The red line highlights the mesoscale flow perturbation, and the yellow line the flow oscillation during C-2.

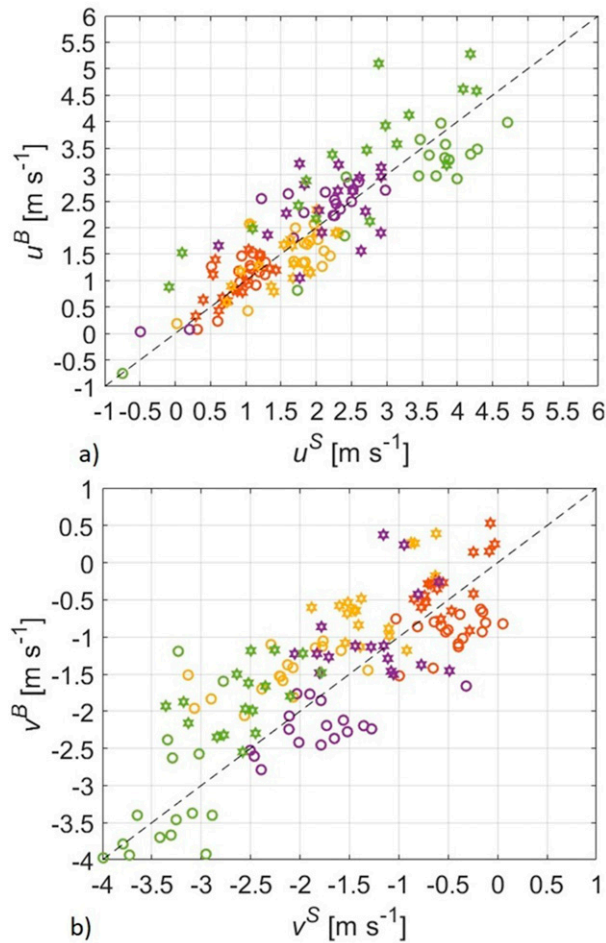


FIG. A1. The 30-min-averaged (a) streamwise and (b) cross-stream wind velocity components comparison between sonic anemometer data on the abscissa and tethered-balloon data (previously interpolated to obtain a regular time series) on the ordinate. Circles encompass the IOP4 night and stars the IOP8 night. Colors identify the observation levels: 2 m in red, 5 m in yellow, 10 m in purple, and 20 m in green.

mostly observed at 2 and 5 m, while the linear dependency mostly encompasses the 10- and 20-m levels. Combining these two aspects, we can define an angle ψ^B associated with the tethered-balloon data as

$$\psi^B = \begin{cases} 0.5(\psi_{2m}^S + \psi_{5m}^S) & \text{if } U_h^B \leq 2 \text{ m s}^{-1} \\ mU_h^B + q & \text{if } U_h^B > 2 \text{ m s}^{-1} \end{cases} \quad (\text{A2})$$

and then compute the ψ -derived wind vertical component w_ψ^B for the tethered balloon as

$$w_\psi^B = U_h^B \tan(\psi^B). \quad (\text{A3})$$

This estimated vertical wind component is compared with the measured one from sonic anemometers in Fig. A2b, giving an overall good match and allowing to compute w_ψ^B along with the whole tethered-balloon profile.

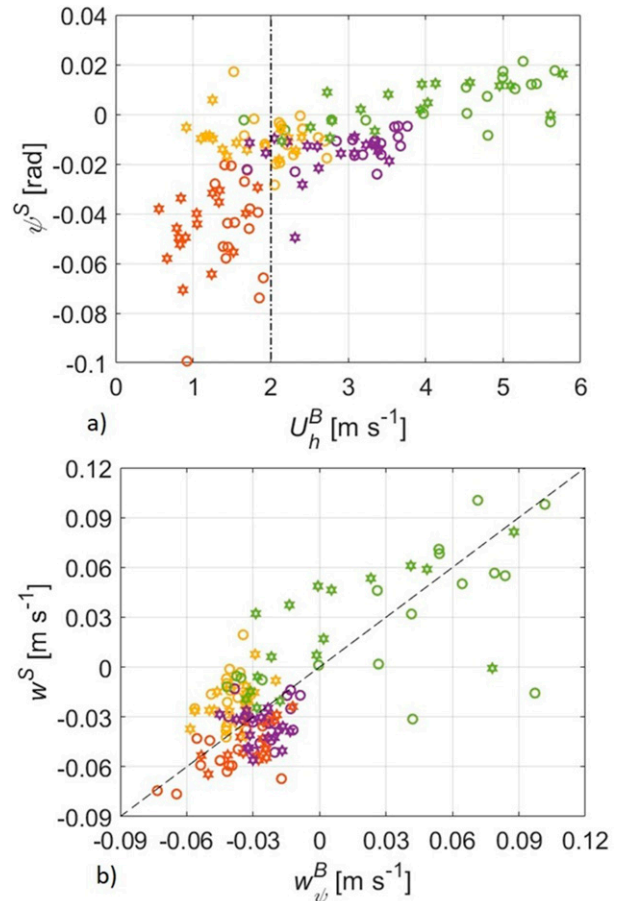


FIG. A2. (a) The 30-min-averaged ψ^S as a function of U_h^B (previously interpolated to obtain a regular time series) and (b) comparison between the 30-min-averaged vertical wind velocity component from the sonic anemometers on the abscissa and the ψ -derived one from tethered balloon on the ordinate. Circles encompass the IOP4 night and stars the IOP8 night. Colors identify the observation levels: 2 m in red, 5 m in yellow, 10 m in purple, and 20 m in green. The vertical dot-dashed line in (a) highlights the $U_h^B = 2 \text{ m s}^{-1}$ threshold.

REFERENCES

- Baas, P., F. C. Bosveld, H. K. Baltink, and A. A. M. Holtslag, 2009: A climatology of nocturnal low-level jets at Cabauw. *J. Appl. Meteor. Climatol.*, **48**, 1627–1642, <https://doi.org/10.1175/2009JAMC1965.1>.
- Banta, R. M., 2008: Stable-boundary-layer regimes from the perspective of the low-level jet. *Acta Geophys.*, **56**, 58–87, <https://doi.org/10.2478/s11600-007-0049-8>.
- , R. K. Newsom, J. K. Lundquist, Y. L. Pichugina, R. L. Coulter, and L. Mahrt, 2002: Nocturnal low-level jet characteristic over Kansas during CASES-99. *Bound.-Layer Meteor.*, **105**, 221–252, <https://doi.org/10.1023/A:1019992330866>.
- , L. S. Darby, J. D. Fast, J. O. Pinto, D. C. Whiteman, W. J. Shaw, and B. W. Orr, 2004: Nocturnal low-level jet in a mountain basin complex. Part I: Evolution and effects on local flows. *J. Appl. Meteor.*, **43**, 1348–1365, <https://doi.org/10.1175/JAM2142.1>.

- Barbano, F., L. Brogno, F. Tampieri, S. Di Sabatino, 2021: Interaction between waves and turbulence within the nocturnal boundary layer. *Bound.-Layer Meteor.*, in press.
- Cava, D., U. Giostra, and G. Katul, 2015: Characteristics of gravity waves over an Antarctic ice sheet during an austral summer. *Atmosphere*, **6**, 1271–1289, <https://doi.org/10.3390/atmos6091271>.
- Du, Y., and G. Chen, 2018: Heavy rainfall associated with double low-level jets over southern China. Part I: Ensemble-based analysis. *Mon. Wea. Rev.*, **146**, 3827–3844, <https://doi.org/10.1175/MWR-D-18-0101.1>.
- , and —, 2019a: Heavy rainfall associated with double low-level jets over southern China. Part II: Convection initiation. *Mon. Wea. Rev.*, **147**, 543–565, <https://doi.org/10.1175/MWR-D-18-0102.1>.
- , and —, 2019b: Climatology of low-level jets and their impact on rainfall over southern China during the early-summer rainy season. *J. Climate*, **32**, 8813–8833, <https://doi.org/10.1175/JCLI-D-19-0306.1>.
- , Q. Zhang, Y. Ying, and Y. Yang, 2012: Characteristics of low-level jets in Shanghai during the 2008–2009 warm seasons as inferred from wind profiler radar data. *J. Meteor. Soc. Japan*, **90**, 891–903, <https://doi.org/10.2151/jmsj.2012-603>.
- Fernando, H. J. S., 2017: Vaisala DigiCORA tethered system data sage brush site, version 1.0. UCAR/NCAR Earth Observing Laboratory, accessed 18 April 2020, <https://doi.org/10.5065/D6XS5SVV>.
- , and Coauthors, 2015: The MATERHORN: Unraveling the intricacies of mountain weather. *Bull. Amer. Meteor. Soc.*, **96**, 1945–1967, <https://doi.org/10.1175/BAMS-D-13-00131.1>.
- Gill, A. E., 1982: *Atmosphere-Ocean Dynamics*. Academic Press, 662 pp., <https://doi.org/10.1002/qj.49711046322>.
- Hoecker, W. H. J., 1963: Three southerly low-level jet systems delineated by the Weather Bureau special pilot network of 1961. *Mon. Wea. Rev.*, **91**, 573–582, [https://doi.org/10.1175/1520-0493\(1963\)091<0573:TSLJSD>2.3.CO;2](https://doi.org/10.1175/1520-0493(1963)091<0573:TSLJSD>2.3.CO;2).
- Hojstrup, J., 1993: A statistical data screening procedure. *Meas. Sci. Technol.*, **4**, 153–157, <https://doi.org/10.1088/0957-0233/4/2/003>.
- Holton, J. R., 2004: *An Introduction to Dynamic Meteorology*. 4th ed. Academic Press, 535 pp.
- Kim, J., and L. Mahrt, 1992: Momentum transport by gravity waves. *J. Atmos. Sci.*, **49**, 735–748, [https://doi.org/10.1175/1520-0469\(1992\)049<0735:MTBGW>2.0.CO;2](https://doi.org/10.1175/1520-0469(1992)049<0735:MTBGW>2.0.CO;2).
- Klein, P., and Coauthors, 2015: LABLE: A multi-institutional, student-led, atmospheric boundary layer experiment. *Bull. Amer. Meteor. Soc.*, **96**, 1743–1764, <https://doi.org/10.1175/BAMS-D-13-00267.1>.
- McMillen, R. T., 1988: An eddy correlation technique with extended applicability to non-simple terrain. *Bound.-Layer Meteor.*, **43**, 231–245, <https://doi.org/10.1007/BF00128405>.
- Pace, J., 2016: Surface atmospheric measurement stations mini network 1 minute average data located to east and south east of granite peak, version 1.0. UCAR/NCAR Earth Observing Laboratory, accessed 18 April 2020, <https://doi.org/10.5065/D6J101K8>.
- , 2017: Dugway proving grounds frequency-modulated continuous-wave (FM/CW) boundary layer radar measurement imagery, version 1.0. UCAR/NCAR Earth Observing Laboratory, accessed 5 May 2020, <https://doi.org/10.5065/D6KW5DG9>.
- , E. Pardyjak, and H. Fernando, 2017: MATERHORN-X tower data, version 1.0. UCAR/NCAR Earth Observing Laboratory, accessed 18 April 2020, <https://doi.org/10.5065/D67W69X5>.
- Pichugina, Y. L., R. M. Banta, and N. D. Kelley, 2007: Analysis of the southern Colorado low-level jet by high resolution Doppler lidar data. Comparison to Great Plains LLJ climatologies. *Third Symp. on Lidar Atmospheric Applications*, San Antonio, TX, Amer. Meteor. Soc., 5.6, https://ams.confex.com/ams/87ANNUAL/techprogram/paper_119093.htm.
- Savage, L., S. Zhong, W. Yao, W. J. Brown, T. W. Horst, and C. D. Whiteman, 2008: An observational and numerical study of a regional-scale downslope flow in northern Arizona. *J. Geophys. Res.*, **113**, D14114, <https://doi.org/10.1029/2007JD009623>.
- Stensrud, D., 1996: Importance of low-level jets to climate: A review. *J. Climate*, **9**, 1698–1711, [https://doi.org/10.1175/1520-0442\(1996\)009<1698:JOLLJT>2.0.CO;2](https://doi.org/10.1175/1520-0442(1996)009<1698:JOLLJT>2.0.CO;2).
- Stull, R. B., 1988: *An Introduction to Boundary Layer Meteorology*. Kluwer Academic, 670 pp.
- Sun, J., and Coauthors, 2002: Intermittent turbulence associated with a density current passage in the stable boundary layer. *Bound.-Layer Meteor.*, **105**, 199–219, <https://doi.org/10.1023/A:1019969131774>.
- , L. Mahrt, C. Nappo, and D. H. Lenschow, 2015a: Wind and temperature oscillations generated by wave–turbulence interactions in the stably stratified boundary layer. *J. Atmos. Sci.*, **72**, 1484–1503, <https://doi.org/10.1175/JAS-D-14-0129.1>.
- , and Coauthors, 2015b: Review of wave-turbulence interactions in the stable atmospheric boundary layer. *Rev. Geophys.*, **53**, 956–993, <https://doi.org/10.1002/2015RG000487>.
- Taylor, J. R., 1997: *An Introduction to Error Analysis: The Study of Uncertainties in Physical Measurements*. 2nd ed. University Science Books, 327 pp., <https://doi.org/10.1063/1.882103>.
- Tuononen, M., E. J. O’Connor, V. A. Sinclair, and V. Vakkari, 2017: Low-level jets over Utö, Finland, based on Doppler lidar observations. *J. Appl. Meteor. Climatol.*, **56**, 2577–2594, <https://doi.org/10.1175/JAMC-D-16-0411.1>.
- Van De Wiel, B. J. H., A. F. Moene, G. J. Steeneveld, P. Baas, F. C. Bosveld, and A. A. M. Holtslag, 2010: A conceptual view on inertial oscillations and nocturnal low-level jets. *J. Atmos. Sci.*, **67**, 2679–2689, <https://doi.org/10.1175/2010JAS3289.1>.
- Viana, S., C. Yagüe, and G. Maqueda, 2009: Propagation and effects of a mesoscale gravity wave over a weakly-stratified nocturnal boundary layer during the SABLES2006 field campaign. *Bound.-Layer Meteor.*, **133**, 165–188, <https://doi.org/10.1007/s10546-009-9420-4>.
- Vickers, D., and L. Mahrt, 1997: Quality control and flux sampling problems for tower and aircraft data. *J. Atmos. Oceanic Technol.*, **14**, 512–526, [https://doi.org/10.1175/1520-0426\(1997\)014<0512:QCAFSP>2.0.CO;2](https://doi.org/10.1175/1520-0426(1997)014<0512:QCAFSP>2.0.CO;2).
- Zhang, M., and Z. Meng, 2019: Warm-sector heavy rainfall in southern China and its WRF simulation evaluation: A low-level-jet perspective. *Mon. Wea. Rev.*, **147**, 4461–4480, <https://doi.org/10.1175/MWR-D-19-0110.1>.